ADVANCED OPTICAL MATERIALS
www.advopticalmat.de

Synergistic Ligand Pair Exchange Strategy in Perovskite Quantum Dots to Enhance Photoelectric Properties and Stability

Xuyang Li, Qihang Lv, Zitong Xu, Weijun Wang, Zhixin Tang, Xia Shen, Zhaohui Shan, Yanqin Miao, Johnny C. Ho, and Pengfei Guo**

Perovskite quantum dots (PeQDs) have attracted significant attention as research materials due to their adjustable bandgaps, high photoluminescence quantum yield, and excellent color purity. However, conventional surface ligands often suffer from weak coordination capacity and low conductivity, adversely affecting the stability and photoelectric properties of PeQDs. In this study, a synergistic ligand pair exchange strategy is introduced to enhance the properties of pristine $CsPbBr_3$ PeQDs. By sequentially incorporating α-methyl-4-fluoro-benzylamine and p-toluenesulfonic acid, the original OA/OAm ligand pair is successfully replaced, efficiently passivating the A- and X-site vacancies. The modified $CsPbBr_3$ PeQDs demonstrate notable improvements in photoluminescence intensity and stability when exposed to UV light, high temperatures, and water immersion. Furthermore, this treatment approach is applicable to $CsPbI_3$ and mixed-halogen PeQDs. A high-performance photodetector fabricated from these treated $CsPbBr_3$ QDs showcases a responsivity of 3.9 mA W^{-1} and a detectivity of 2.0×10^{10} Jones, representing a 6-fold enhancement over untreated counterparts. Also, devices based on treated $CsPbBr_3$ QDs show potential in optical communications, effectively illustrating encryption and decryption processes. This synergetic ligand pair exchange strategy offers a promising avenue for the broader application of PeQDs in optoelectronics devices and circuits.

1. Introduction

Perovskite quantum dots (PeQDs) have become a focal point in research due to their remarkable attributes, including high photoluminescence quantum yield, narrow emission spectra, tunable wavelengths, and cost-effectiveness. These characteristics make PeQDs ideal candidates for various optoelectronic applications, such as solar cells, light-emitting diodes, photodetectors, lasers, and scintillators.[1–7] Compared to perovskite films, PeQDs benefit from a higher density of surface ligands, which help prevent agglomeration and mitigate surface defects.[8–10] However, commonly used organic ligands like oleylamine (OAm) and oleic acid (OA) suffer from low conductivity and weak coordination with perovskite materials.[11,12] Moreover, these ligands are prone to desorption during the assembly of semiconducting solids, leading to poor charge transport and increased nonradiative recombination.[13,14] Consequently, devices based on PeQDs often underperform in efficiency and stability compared to those utilizing perovskite films.[15]

To address these challenges, various strategies have been explored to enhance the photoelectric properties and stability of PeQDs.[16–22] For example, Dong et al. introduced an excess halide source during PeQD synthesis to modulate crystallization and growth kinetics, improving fluorescence intensity and color purity.[23] Zeng et al. replaced OA with benzenesulfonic acid, whose halide-equivalent sulfonate ion strongly binds with lead ions, significantly boosting optical properties and thermal stability.[24] Despite these advances, long alkyl chain ligands constrain carrier transport in PeQD-based devices.[9,25,26] Recent post-synthetic treatments have aimed to enhance conductivity by swapping long insulating ligands for shorter, high-affinity alternatives. Jeon et al. demonstrated that treating colloidal quantum dots with $NOBF_4$, which has a higher binding energy with perovskite, replaces OA and replenishes trap sites, resulting in a 2.8-fold increase in light-emitting diode efficiency.[27] Li et al. employed diphenylphosphoryl azide to modify PeQD surfaces, using the generated diphenyl phosphate to improve carrier transport through π-conjugated benzene rings.[28] Despite these promising developments, most current methods focus primarily on replacing OA with anionic or neutral ligands, with limited attention given to organic ammonium and the synergistic regulation of ligand pairs on PeQD surfaces.

X. Li, Q. Lv, Z. Xu, Z. Tang, Z. Shan, Y. Miao, P. Guo
College of Physics and Optoelectronics
Taiyuan University of Technology
Taiyuan 030024, China
E-mail: guopengfei@tyut.edu.cn

X. Shen
School of Basics
Shanxi Institute of Energy
Taiyuan 030024, China
E-mail: sx2025@sxie.edu.cn

W. Wang, J. C. Ho
School of Materials Science and Engineering
City University of Hong Kong
Hong Kong 999077, China

The ORCID identification number(s) for the author(s) of this article can be found under https://doi.org/10.1002/adom.202502489

DOI: 10.1002/adom.202502489

In this work, we introduce a synergetic ligand pair exchange (SLPE) strategy to enhance the photoelectric properties and stability of $CsPbBr_3$ PeQDs. The SLPE strategy is realized by sequentially adding α-methyl-4-fluoro-benzylamine (F-MBA) and p-toluenesulfonic acid (*p*-TsA) into purified PeQDs solutions. This process relies on two key mechanisms: the acidity of *p*-TsA modulates the dynamic equilibrium of the original OA/OAm pair, and the resulting F-MBA$^+$ and *p*-TsO$^-$ ions bind tightly to the surface of the $CsPbBr_3$ PeQDs, which enables the ligand exchange and passivation of surface defects. Photoluminescence spectra reveal that individually adding F-MBA and *p*-TsA has negligible or negative impacts on PL intensity. However, their sequential addition leads to a remarkable 2.5-fold increase in PL intensity. Furthermore, the treated PeQDs exhibit enhanced stability under UV exposure, high temperatures, and water immersion. The SLPE strategy is also applicable to optimizing other PeQD compositions. Photodetectors fabricated from these modified $CsPbBr_3$ QDs show a photocurrent of 5.1 nA, a responsivity of 3.9 mA W^{-1}, and a detectivity of 2.0×10^{10} Jones, marking a significant improvement over devices based on untreated $CsPbBr_3$ QDs. Furthermore, these photodetectors demonstrate potential in optical communications, effectively illustrating encryption and decryption processes. The SLPE strategy offers a promising avenue for optimizing perovskite QDs and expanding their applications in diverse optoelectronic devices.

2. Results and Discussion

2.1. The Synthesis and Optimization of the SLPE Strategy Treated $CsPbBr_3$ QDs

The $CsPbBr_3$ QDs are synthesized by a conventional hot injection method with modifications;[29,30] the complete procedures are described and shown in the Experimental Section. Through a crude centrifugation, the F-MBA and *p*-TsA, whose chemical structure is shown in Figure S1 (Supporting Information), are added to the colloidal $CsPbBr_3$ QDs solution, and their influence on the PL spectrum is observed. First, as a strong Lewis acid, the individual addition of *p*-TsA will lead to the serious disruption of the original reaction equilibrium between OA and OAm according to the equation below:

$$p-\mathrm{TsA}+\mathrm{OAm}\rightarrow p-\mathrm{TsO}^{-}+\mathrm{OAm}^{+} \tag{1}$$

$$\mathrm{OA}^{-}+\mathrm{OAm}^{+}\rightarrow \mathrm{OA}+\mathrm{OAm} \tag{2}$$

which induce the rapid detachment of ligands and distinct fluorescence quenching of $CsPbBr_3$ QDs (Figure S2, Supporting Information).[31] On the other hand, the F-MBA has a negligible effect on the optical property of $CsPbBr_3$ QDs even though the ligand content and reaction time are increased (Figure S3, Supporting Information).[32,33] By contrast, following the successive treatment with F-MBA and *p*-TsA, the F-MBA can react with *p*-TsA in the equation below:

$$p-\mathrm{TsA}+\mathrm{F}-\mathrm{MBA}\rightarrow p-\mathrm{TsO}^{-}+\mathrm{F}-\mathrm{MBA}^{+} \tag{3}$$

resulting in weakening the acidity and retard the desorption of OA/OAm, meanwhile, the strong affinity of F-MBA$^+$ and *p*-TsO$^-$ will tightly bind on the surface of $CsPbBr_3$ QDs to realize the ligand exchange and defect reparation. Additionally, a one-fold improvement in the PL intensity is realized by optimizing the feeding amount of additives (Figure S4, Supporting Information). All these experimental results shed light on the significance of the SLPE strategy for the modulation of the optical properties of PeQDs.

The pristine $CsPbBr_3$ QDs (denoted as P-QDs) and SLPE-treated $CsPbBr_3$ QDs (denoted as SLPE-QDs) are finally obtained after the second purification with ethyl acetate to remove the excess ligands and impurities. The UV–vis absorption spectrum of P-QDs and SLPE-QDs is similar. At the same time, the PL intensity of SLPE-QDs is 2.5 times larger than that of the P-QDs (**Figure 1**a), and the shorter tail is observed in the PL spectra of SLPE-QDs (Figure S5, Supporting Information), which indicates the effective defect passivation and stable binding of ligands for the surface of SLPE-QDs.[34] Moreover, the SLPE-QDs effectively reduce the Urbach energy (E_u) to 18 meV, compared with the E_u of 20 meV for the P-QDs (Figure 1b). Such a lowered E_u commonly demonstrates a reduced number of band-edge trap states.[35,36] The time-resolved PL (TRPL) decay measurements are conducted to investigate the radiative recombination kinetics of photogenerated carriers. The SLPE-QDs achieve a longer PL lifetime constant of 43.7 ns with a mono-exponential decay. In contrast, the P-QDs show a bi-exponential decay TRPL curve with a lifetime constant of 23.5 ns (Figure 1c; Table S1, Supporting Information). The transition of the PL decay kinetics from bi-exponential to mono-exponential behavior manifests the efficient suppression of trap-mediated recombination via the SLPE strategy.[37,38]

Figure 1d,e exhibits the transmission electron microscopy (TEM) images of P-QDs and SLPE-QDs respectively, which display a uniform crystal with cubic morphology, indicating a minimal influence on the morphology of $CsPbBr_3$ QDs after the SLPE treatment. To obtain more information on the crystal structure of P-QDs and SLPE-QDs, high-resolution TEM (HRTEM) characterizations are performed, and a lattice constant of 0.29 nm is obtained for both QDs, corresponding to the (200) facets of the orthorhombic phase of $CsPbBr_3$[39,40] The X-ray diffraction (XRD) results also show the most intense (100) and (200) crystal plane diffraction peaks (Figure 1f), further supporting that SLPE-QDs have the same crystal structure as P-QDs.[41,42]

2.2. Surface Chemistry Characterization of P-QDs and SLPE-QDs

The surface coordination environment of P-QDs and SLPE-QDs is investigated through X-ray Photoelectron Spectroscopy (XPS) and Fourier Transform Infrared Spectroscopy (FTIR) analysis (**Figure 2**). The signal of S is only detected for the SLPE-QDs, confirming the successful replacement of OA$^-$ with *p*-TsO$^-$ (Figure 2a). The Pb 4f spectra of P-QDs exhibit two contributions, $4f_{7/2}$ and $4f_{5/2}$, located at 138.0 and 142.9 eV, after modification by F-MBA and *p*-TsA, a 0.3 eV shift to the higher binding energy of 138.3 and 143.2 eV is observed for the Pb 4f spectra of SLPE-QDs (Figure 2b). And the Br 3d spectra of SLPE-QDs also show a shift of 0.4 eV to the higher binding energy (Figure S6a, Supporting Information), which can be attributed to the strong coordination ability of sulfonate with Pb^{2+}.[24,43] It is worth noting that there is

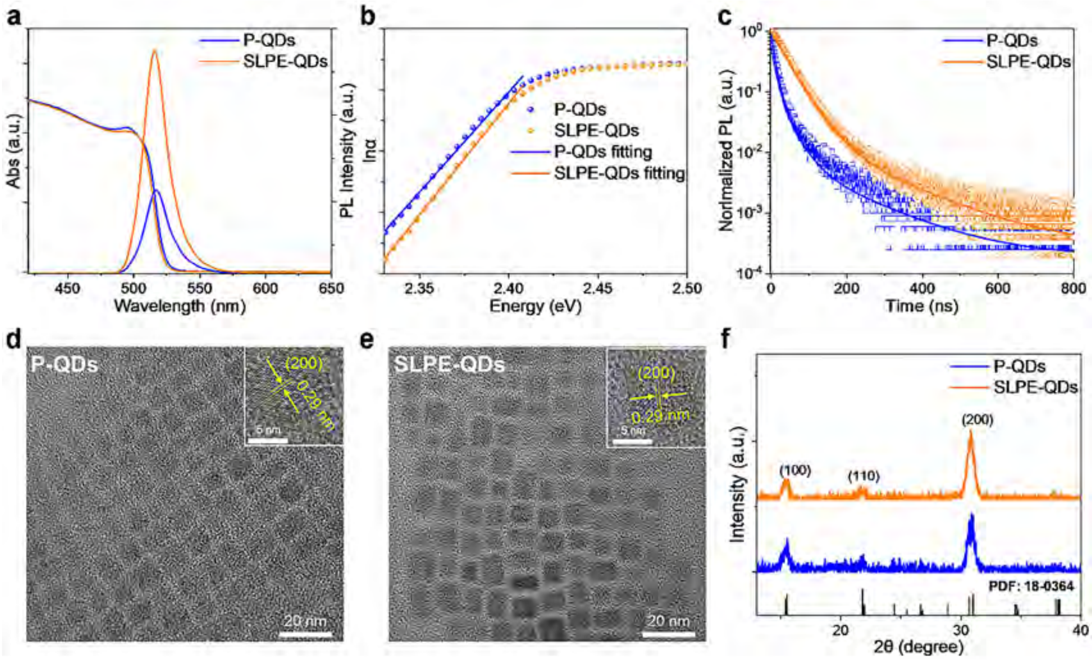

Figure 1. Optical properties and crystal structural characteristics of P-QDs and SLPE-QDs. a) The absorption spectra and PL spectra of P-QDs and SLPE-QDs, respectively. b) Logarithm of absorption coefficient α versus photon energy of P-QDs and SLPE-QDs. c) The TRPL curve of P-QDs and SLPE-QDs. d,e) The TEM and HR-TEM (insets) images of P-QDs and SLPE-QDs. f) The XRD pattern of these P-QDs and SLPE-QDs, respectively.

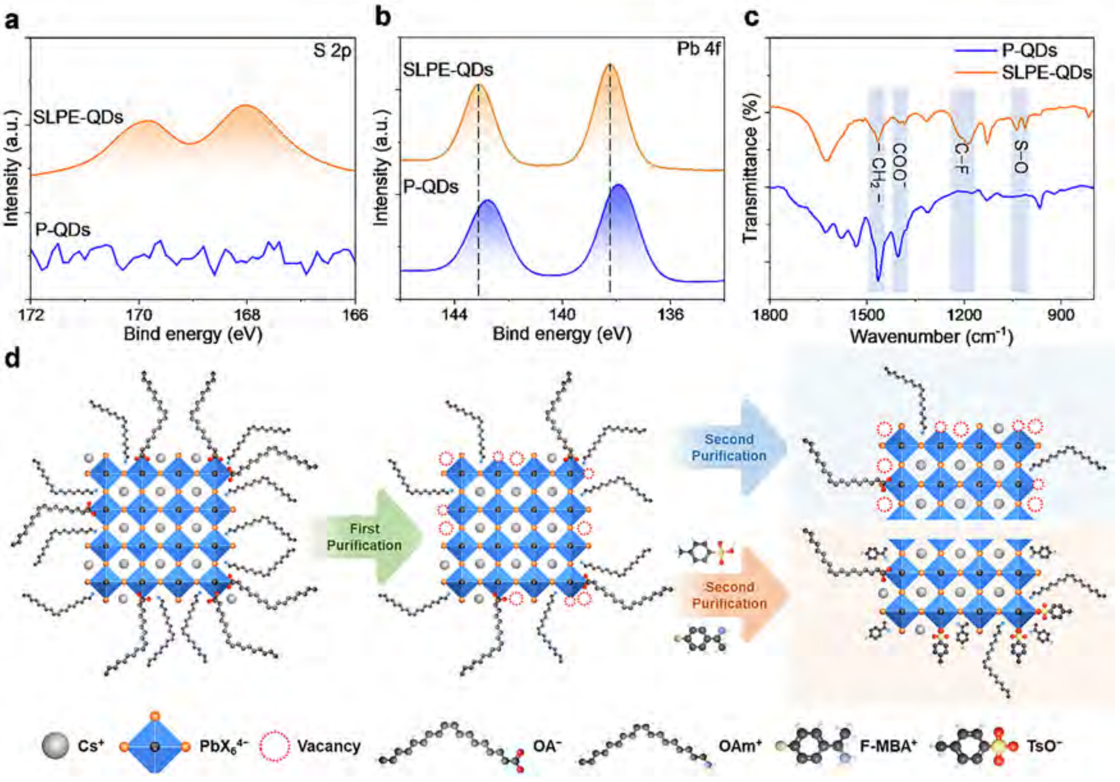

Figure 2. Surface chemistry investigation for P-QDs and SLPE-QDs. High-resolution XPS spectra of a) S 2p and b) Pb 4f for P-QDs (orange line) and SLPE-QDs (blue line), respectively. c) Corresponding FTIR spectra of P-QDs and SLPE-QDs. d) Schematic illustration of the PeQDs treated with and without the SLPE strategy.

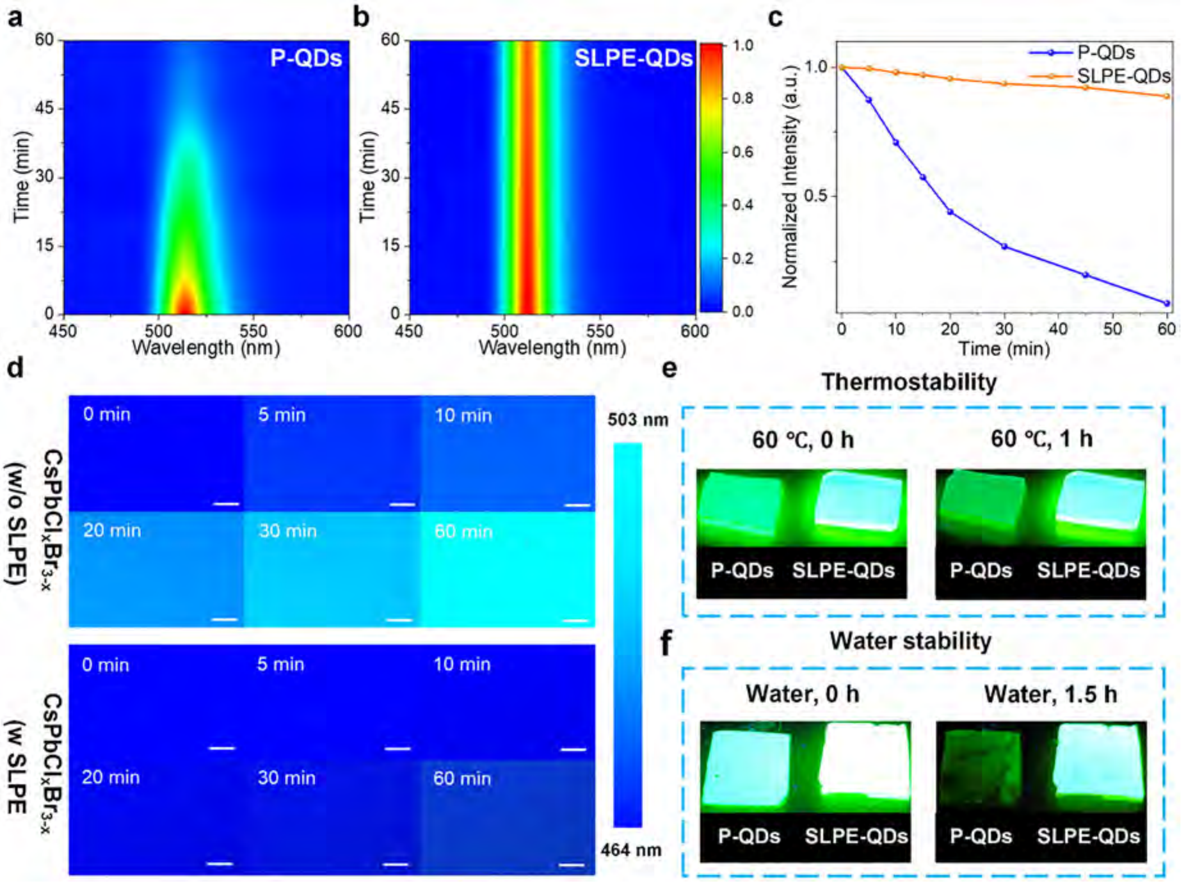

Figure 3. The stability measurements of P-QDs and SLPE-QDs. a,b) The evolution of PL spectra of P-QDs and SLPE-QDs under continuous 375 nm light irradiation with a power density of 30 W cm^{-2}. c) The evolution of PL intensity with increased irradiation time for P-QDs and SLPE-QDs under a 375 nm laser illumination, respectively. d) Dark-field emission images of CsPbCl$_x$Br$_{3-x}$ films treated without and with SLPE strategy with different 375 nm light (30 W cm^{-2}) irradiation times, respectively (scale bar: 50 µm). e,f) Photographs of P-QDs and SLPE-QDs film heating at 60 °C and soaking in water under UV light illumination.

a minor variation of the Cs-3d core level spectrum, indicating the negligible influence of SLPE treatment on the coordination environment of Cs$^+$ (Figure S6b, Supporting Information). Fourier transform infrared spectroscopy (FTIR) of P-QDs and SLPE-QDs is also measured to observe the variation of surface ligands further. As shown in Figure 2c, two distinctive signals are detected at 1038 and 1013 cm^{-1} for the FTIR of SLPE-QDs, which can be attributed to the S−O stretching vibrations. A signal of the C−F is observed at 1186 cm^{-1}, indicating the effective binding of F-MBA$^+$ and *p*-TsO$^-$ on the surface of PeQDs.[44,45] The bending vibrations signal of −CH$_2$− at 1465 cm^{-1} and symmetric stretching vibrations signal of −COO$^-$ at 1390 cm^{-1} are observed for both P-QDs and SLPE-QDs,[46] and their signal intensity is reduced for SLPE-QDs, confirming the efficient replacement ligand pair of OA/OAm with F-MBA$^+$/*p*-TsO$^-$. Besides, the residual OA and OAm support the dispersibility of CsPbBr$_3$ QDs.[25,47] According to the above measurement results, a schematic illustration of the SLPE strategy is proposed in Figure 2d. After the first purification of originally synthesized PeQDs, some surface defects are generated. With the continuous addition of F-MBA and *p*-TsA, the surface OA/OAm ligand pair and defects are replaced and passivated by the F-MBA$^+$/*p*-TsO$^-$. Experienced the second purification, the P-QDs exhibit more surface defects due to the weak binding between OA/OAm with perovskite; inversely, the strong coordination ability of F-MBA$^+$/p-TsO$^-$ makes SLPE-QDs have a high ligand density, so the PL intensity of SLPE-QDs is much higher than that of P-QDs. Encouraging the effectiveness of the SLPE strategy, the CsPbI$_3$ and mixed-halogen PeQDs are also treated with the same method, exhibiting the improvement of optical properties (Figure S8, Supporting Information).

2.3. Stability Measurements of P-QDs and SLPE-QDs

Perovskite materials are sensitive to the external environmental factors due to their soft lattice and low formation energy.[48–50] Furthermore, the surface defect site will accelerate the decomposition of PeQDs.[51] To evaluate the contribution of SLPE strategy treatment for the stability of PeQDs, the P-QDs and SLPE-QDs are subjected to diverse external stimuli. Photodegradation and photo-induced phase separation of PeQDs are common phenomena and have been documented in the previous literature.[52,53] As shown in **Figure** 3a–c, the PL intensity of P-QDs solution shows a dramatic drop of 91% after 60 min of continuous UV

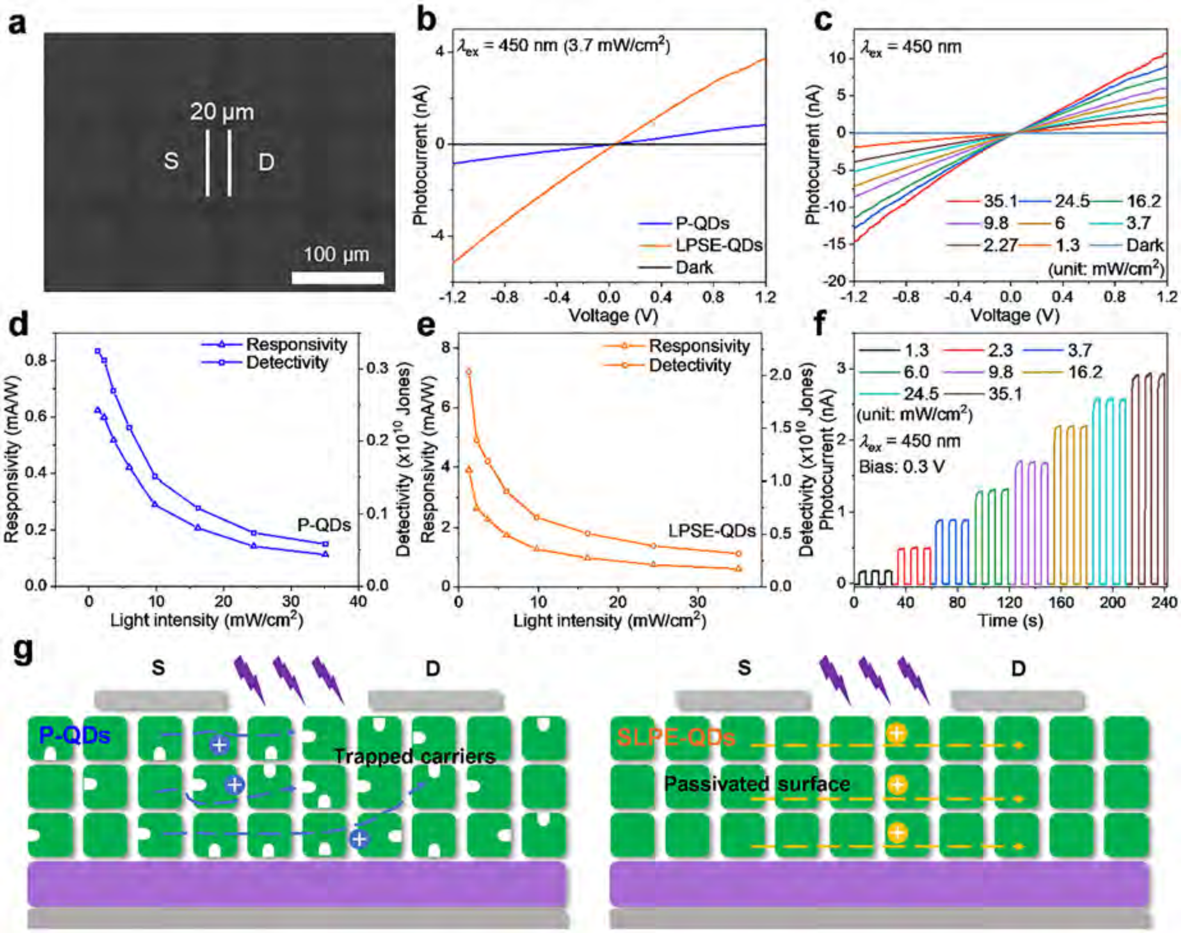

Figure 4. Optoelectronic characterization of P-QDs and SLPE-QDs based photodetectors. a) SEM image of SLPE-QDs-based photodetector. (S, source electrode; D, drain electrode.) b) The *I–V* curve of the photodetector based on P-QDs and SLPE-QDs under a 450 nm laser excitation with a power density of 3.7 mW cm^{-2}. c) Power density dependent *I–V* curve of SLPE-QDs photodetector under a 450 nm laser illumination. d,e) The responsivity and detectivity of photodetectors based on the P-QDs and SLPE-QDs. f) Photoresponse curves of the SLPE-QDs photodetector at 0.3 V bias for different laser intensities. g) Schematic diagram of charge transport of P-QDs and SLPE-QDs photodetectors, respectively.

exposure (375 nm, 30 W cm^{-2}), while the SLPE-QDs solution still maintains the stable green emission with only a slight fluorescence attenuation (11%). Besides, there is a little red shift of PL spectra for CsPbCl$_x$Br$_{3-x}$ QDs film treated with SLPE strategy under continuous irradiation with a 375 nm laser (30 W cm^{-2}). In comparison, a ≈ 40 nm (0.2 eV) red shift is observed for the untreated CsPbCl$_x$Br$_{3-x}$ QDs film under the same conditions (Figure 3d; Figure S9, Supporting Information). The enhanced photostability of SLPE-QDs originates from the effective passivation of surface vacancies and stable binding of F-MBA$^+$ and *p*-TsO$^-$ with perovskite. Subsequently, we check the thermal stability of P-QDs and SLPE-QDs by placing the corresponding film on the 60 °C hot plate and capturing images under daylight and UV light at different heating times (Figure 3e; Figure S10, Supporting Information). The P-QDs film exhibits the obvious decay of luminescence under UV light for 1 h heating, while the SLPE-QDs film remains bright under the same conditions. Finally, considering the humidity-sensitive characteristic of perovskite materials, the sample film is immersed in water.[54] The P-QDs film becomes almost nonluminous under UV light illumination after soaking in water for 1.5 h; conversely, there is a mere weakening of fluorescence for the SLPE-QDs film (Figure 3f; Figure S11, Supporting Information). The significant amelioration of stability against water for SLPE-QDs may be ascribed to the hydrophobicity of the fluorine atom in the ligand of F-MBA$^+$.[55]

2.4. Performance Measurements of Photodetectors Based on the P-QDs and SLPE-QDs

The long aliphatic chain of OA/OAm leads to the inferior conductivity and affects the application of PeQDs in photoelectric devices,[9,13] when the PeQDs are modified with the SLPE strategy, the short and conjugated molecular structure of F-MBA$^+$ and *p*-TsO$^-$ will promote the charge transfer. To determine the improvement of overall conductivity for SLPE-QDs, the photodetector with an architecture of Si/SiO$_2$/PeQDs film/electrode is fabricated, where the channel length is 20 μm (**Figure 4**a; Figure S13, Supporting Information). Figure 4b shows the current–voltage (I–V) curve of the P-QDs and SLPE-QDs photodetector under a 450 nm laser excitation with a power density of 3.7 mW cm^{-2}. The slope of the I–V curve of the SLPE-QDs device is much higher than that of the P-QDs device, suggesting the enhancement of in-plane carrier mobility (Figure S14a, Supporting Information).[56,57] Figure 4c and Figure S14b (Supporting Information) are the I–V curves of SLPE-QDs- and P-QDs-based photodetectors excited by the 450 nm laser with different power densities. The photocurrent gradually augments with the increase of applied bias and laser intensity. The responsivity (R) and detectivity (D^*) are calculated according to the equation below:

$$R = \frac{I_{light} - I_{dark}}{PA} \tag{4}$$

$$D^* = R\sqrt{\frac{A}{2eI_{dark}}} \tag{5}$$

where I_{light} and I_{dark} denote as the photocurrent under a UV light illumination and dark, P is the power density of excitation light, A is the effective illuminated area, and e is the electronic charge. A maximum R of 3.9 mA W^{-1} and D^* of 2.0×10^{10} Jones is obtained for the SLPE-QDs photodetector under a 450 nm laser illumination with the power density of 1.3 mW cm^{-2} at the bias of 1.2 V (Figure 4d). By contrast, the PQDs photodetector only exhibits a maximum R of 0.6 mA W^{-1} and D^* of 0.32×10^{10} Jones under the same conditions (Figure 4e). It is noted that the R of devices exhibits a decay with the increase of light power density, which may be derived from the enhanced Auger recombination rate of photogenerated carriers and the shortened carrier lifetime under higher power density.[58] Figure 4f and Figure S14c (Supporting Information) show the time-dependent current of on–off cycles at 0.3 V bias with variable light intensities. The photocurrent exhibits a rapid rise upon irradiation, and the SLPE-QDs photodetector has a lower rise time of 32 ms (Figure S15, Supporting Information), suggesting the quick separation and transfer of photogenerated carriers. Both photodetectors show a drastic photocurrent decay to the original value when the laser is turned off. The operation stability of photodetectors based on the P-QDs and SLPE QDs is evaluated after 100 on/off switching cycle measurement. The photocurrent of P-QDs photodetectors exhibits a 46% reduction, while the photodetectors based on SLPE-QDs have a slight attenuation (≈6%) in photocurrent (Figure S16 Supporting Information). According to the above results, a model schematic diagram is presented to describe the impacts of SLPE treatment on the charge transfer of PeQDs, as shown in Figure 4g. For the P-QDs, the weak and dynamic binding of surface ligands will inevitably lead to the detachment of OA/OAm and the generation of trap states during the process of spin-coating of PeQDs, combined with the worse conductivity of the long alkyl chain ligands, the lower photocurrent is observed for the P-QDs photodetector. For comparison, F-MBA^+ and p-TsO^- have an excellent conductivity due to their short and conjugated molecular structure; meanwhile, the strong affinity of F-MBA^+ and p-TsO^- with the perovskite will produce a stable surface for SLPE-QDs. Hence, the photodetector based on SLPE-QDs exhibits an improved device performance, comparable with previous reports (Table S2, Supporting Information).

2.5. The Application of SLPE-QDs in Optical Communication

To expand the application of SLPE-QDs, an encryption/decryption optical communication system based on a wavelength-tunable SLPE-QDs device is fabricated. As shown in **Figure 5a**, encrypted information is generated and represented as the photocurrent by the simultaneous utilization of 405 and 450 nm lasers, and the photoresponse of SLPE-QDs-based photodetectors under 405 and 450 nm lasers illumination is shown in Figure S17 (Supporting Information). After the acquisition of the photocurrent signal of the key, the original photocurrent signal and the corresponding right information will be decrypted. For example, the ASCII code of the initial signal for the "PeQD" word is represented by positive "0" and "1" signals using a 450 nm laser. The key information of the "NICE" word is represented by positive "0" and "1" using a 405 nm CW laser. Through the synergistic operation of light sources of 405 and 450 nm laser on the SLPE-QDs photodetector, an encrypted electrical output signal is recorded as shown in Figure 5b, combined with the key signal of word "NICE" (mid in Figure 5b), the original information of "PeQD" is restored to realize a cycle of encryption and decryption communications as shown in Figure 5b.

3. Conclusion

In summary, we have successfully developed a ligand pair synergetic exchange strategy to enhance the surface properties of PeQDs. By sequentially introducing high-affinity ligands into purified PeQDs solutions, we achieved effective replacement of OA/OAm and passivation of surface defects. This approach leads to notable improvements in optical properties without altering the morphology or crystal structure of the PeQDs. Furthermore, SLPE-QDs demonstrate remarkable stability when subjected to external conditions such as UV exposure, high temperatures, and water immersion. This strategy is versatile and applicable to optimizing PeQDs with various compositions. High-performance photodetectors fabricated using SLPE-QDs exhibit significantly enhanced photocurrent, with a maximum responsivity of 3.9 mA W^{-1} and detectivity of 2.0×10^{10} Jones, representing a 6-fold increase compared to photodetectors based on untreated PeQDs. Importantly, SLPE-QDs show potential in optical communications, effectively facilitating encryption and decryption processes. Our work presents a viable method for improving the photoelectric properties and stability of PeQDs, thereby broadening their applications across diverse optoelectronic devices.

4. Experimental Section

Materials: Oleic acid (OA, 90%), oleylamine (OAm, 80%–90%), 1-octadecene (ODE, >90.0%), ethyl acetate (EtOAc, anhydrous, 99.5%), N,N-dimethylformamide (DMF, 99.8%), and toluene (Tl, 99.5%) were purchased from Aladdin. Cesium carbonate (Cs_2CO_3, >99.99%) and Octane

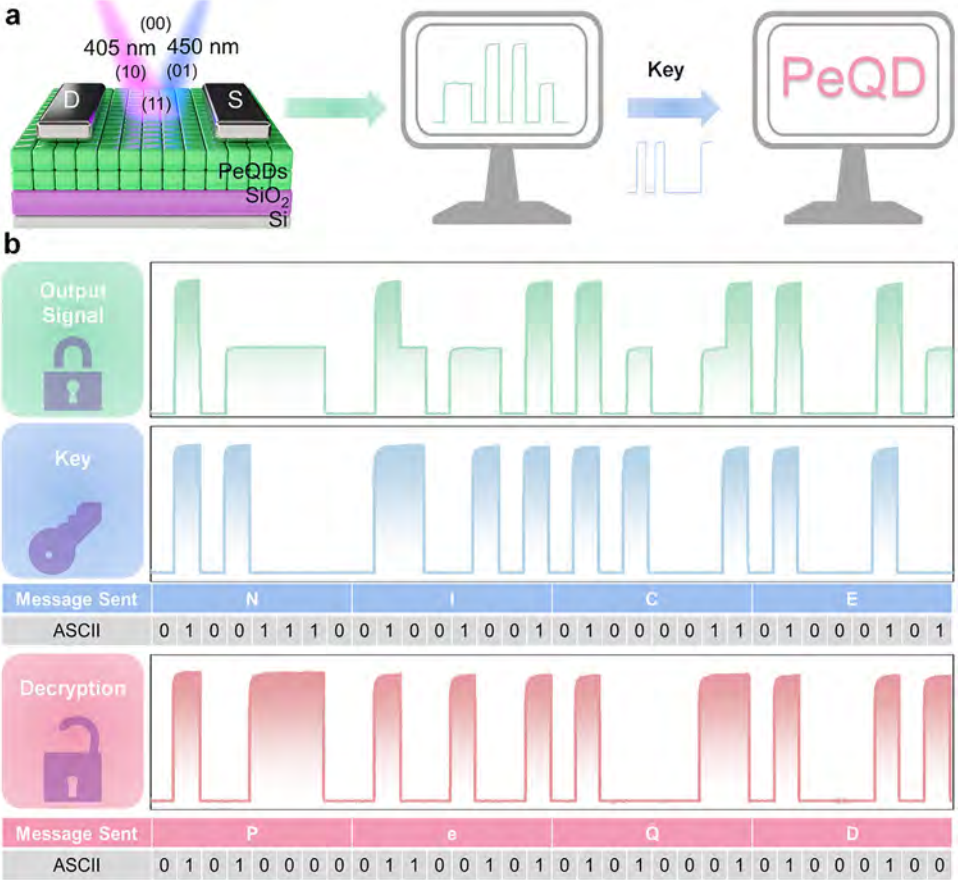

Figure 5. The application of SLPE-QDs photodetector in optical communication. a) Schematic diagrams of the encryption/decryption optical communication system based on the wavelength-tunable SLPE-QDs device. b) The encrypted electrical signal obtained from the wavelength-tunable SLPE-QDs photodetector (top); The electrical key of "NICE" word converted from optical signal through ACSII (mid); Decrypted electrical signal of "PeQD" word by treating the output signal with the key.

(Oc, > 98%) were obtained from Alfa Aesar. *p*-Toluenesulfonic acid (*p*-TsA, 99%), *α*-methyl-4-fluoro-benzylamine (F-MBA, 98%), and lead bromide ($PbBr_2$, 99.9%) were purchased from Macklin. All chemicals were utilized as received without further purification.

Preparation of Cesium Oleate (CsOA): Cs_2CO_3 (100 mg), ODE (5 mL), and OA (0.4 mL) were loaded into a 50 mL 3-neck flask and dried under a vacuum condition for 30 min at RT and 30 min at 120 °C. The mixture was then heated at 120 °C in an argon atmosphere until no bubbles were formed. The synthesized CsOA solution was rapidly collected in a vial with argon protection and was again heated to 100 °C for later use.

Preparation of Perovskite Quantum Dots: 0.69 mg of $PbBr_2$, 0.5 mL of OA, 0.5 mL of OAm, and 5 mL ODE were added to a 100 mL 3-neck flask. The mixture was degassed for 60 min at 100 °C, then the temperature was increased to 120 °C to ensure the complete dissolution of $PbBr_2$. When the temperature was further raised to 170 °C, the CsOA precursor (0.4 mL) was instantly injected into the reaction mixture, and $\approx$ 5 s later, the flask was quickly cooled down to RT by soaking the flask in an ice-water bath.

Purification of Perovskite Quantum Dots: EtOAc was added to the crude solution with a volume ratio of 2:1, and the precipitate was dispersed in 6 mL of Tl. The purification procedure was repeated once, and the precipitate was redispersed in 3 mL Oc to obtain the pristine perovskite quantum dots (P-QDs). For the SLPE-QDs, the first-purification perovskite quantum dots were continuously treated with 0.15 mL of F-MBA (0.3 м in Tl) and 0.15 mL of *p*-TsA (0.3 м in DMF/Tl (v/v = 1:9)). After the second purification under the same conditions as P-QDs, the SLPE-QDs were acquired.

Materials Characterization: The PL spectra were obtained from a home-built confocal micro-optical system with an Ocean Optics Spectrometer (Maya Pro2000) and an excitation wavelength of 375 nm. The QDs morphology, size, and crystal structures were obtained using a transmission electron microscope (TEM, JEM-F200) operated at 200 kV. The powder X-ray diffraction pattern was acquired by X-ray Diffractometer (SmartLab 9 kW, Rigaku) with Cu K*α* radiation (λ = 1.54178 Å). Time-resolved PL decay curves were monitored with an Edinburgh FLS1000 using a 355 nm laser. X-ray photoelectron spectroscopy (XPS) analysis was conducted with a Thermo ESCALAB 250Xi system, and a He UV-light (21.22 eV) was employed as the excitation source. Fourier transform infrared (FTIR) measurements were conducted by a Fourier Transform Infrared Spectrometer (Nicolet 6700) in a transmittance mode. The surface morphology of the photodetector device was analyzed through scanning electron microscopy (SEM, Hitachi SU-8010, Japan).

Fabrication and Measurements of Photodetector Devices: The SiO_2/Si substrates were cleaned through sequential sonication in deionized water, acetone, and 2-isopropanol for 10 min. The P-QDs and SLPE-QDs solution underwent three spin-coating cycles at 1000 rpm for 60 s. Thermal evaporation (SLZF 270) was used to deposit electrode layers with a thickness of 200 nm under a high vacuum of $\approx 4 \times 10^{-4}$ Pa. Device measurements were conducted on the electrical probe station in an atmosphere, and the *I–V* and *I–T* curves were recorded with a Keithley 2450 semiconductor analyzer. The power density of incident light was measured by a CNI-Laser-TP100 power meter, and its intensity was adjusted by an attenuating lens (OMMB-NDFC5020).

Calculation of Urbach Energies (E_U): Urbach energies (E_U) of the P-QDs and SLPE-QDs are calculated by plotting the absorption coefficient as a function of photon energy. The E_U is defined as $E_U = k_B T/\sigma(T)$, which can be extracted by fitting the exponential part of the Urbach tail according to the following equation:

$$\alpha(E) = \alpha_0 \exp\left[\sigma(T)\frac{E - E_0}{k_B T}\right] \tag{6}$$

where k_B is the Boltzmann constant, T represents the absolute temperature, $\alpha(E)$ is the absorption coefficient as a function of photon energy E, E_0 and α_0 are the characteristic parameters, and $\sigma(T)$ is the steepness parameter.[35,36]

Supporting Information

Supporting Information is available from the Wiley Online Library or from the author.

Acknowledgements

X.Y.L. and Q.H.L. contributed equally to this work. The authors thank the National Natural Science Foundation of China (No. 52373246).

Conflict of Interest

The authors declare no conflict of interest.

Data Availability Statement

The data that support the findings of this study are available from the corresponding author upon reasonable request.

Keywords

encrypted communication, ligand exchange, perovskite quantum dots, stability

Received: July 30, 2025
Revised: October 1, 2025
Published online: October 17, 2025

[1] M. V. Kovalenko, L. Protesescu, M. I. Bodnarchuk, *Science* **2017**, *358*, 745.
[2] S. Yakunin, L. Protesescu, F. Krieg, M. I. Bodnarchuk, G. Nedelcu, M. Humer, G. De Luca, M. Fiebig, W. Heiss, M. V. Kovalenko, *Nat. Commun.* **2015**, *6*, 8056.
[3] X. Zhang, H. Huang, C. Zhao, J. Yuan, *Chem. Soc. Rev.* **2025**, *54*, 3017.
[4] Y. Tang, Y. Jing, T. C. Sum, A. Bruno, S. G. Mhaisalkar, *Adv. Energy Mater.* **2025**, *15*, 2400322.
[5] Q. Zhang, D. Zhang, B. Cao, S. Poddar, X. Mo, Z. Fan, *ACS Nano* **2024**, *18*, 8557.
[6] A. Anand, M. L. Zaffalon, A. Erroi, F. Cova, F. Carulli, S. Brovelli, *ACS Energy Lett.* **2024**, *9*, 1261.
[7] Q. Zeng, S. Hwang, H. Kim, T.-W. Lee, *Natl. Sci. Rev.* **2025**, *12*, nwaf135.
[8] J. S. Kim, J.-M. Heo, G.-S. Park, S.-J. Woo, C. Cho, H. J. Yun, D.-H. Kim, J. Park, S.-C. Lee, S.-H. Park, E. Yoon, N. C. Greenham, T.-W. Lee, *Nature* **2022**, *611*, 688.
[9] Y.-H. Kim, T.-W. Lee, *Accounts Mater. Res.* **2023**, *4*, 655.
[10] J. Shamsi, G. Rainò, M. V. Kovalenko, S. D. Stranks, *Nat. Nanotechnol.* **2021**, *16*, 1164.
[11] L. De Trizio, I. Infante, L. Manna, *Acc. Chem. Res.* **2023**, *56*, 1815.
[12] N. Fiuza-Maneiro, K. Sun, I. López-Fernández, S. Gómez-Graña, P. Müller-Buschbaum, L. Polavarapu, *ACS Energy Lett.* **2023**, *8*, 1152.
[13] H. Aqoma, S.-H. Lee, I. F. Imran, J.-H. Hwang, S.-H. Lee, S.-Y. Jang, *Nat. Energy* **2024**, *9*, 324.
[14] H. Ma, E. Ahn, D. Lee, H. Kim, K. Lee, H. C. Lee, S. Lee, S. Ji, K. Kim, H. Ahn, H. Zheng, J. Yang, *Matter* **2025**, *8*, 102083.
[15] S. J. Kim, M. A. Khan, D. G. Lee, T. H. Kim, M. J. Lee, Y. Kang, M. Yang, H. Ahn, K. Park, T. K. Lee, J. W. Shim, *Adv. Funct. Mater.* **2025**, *35*, 2423796.
[16] J.-N. Yang, J.-J. Wang, Y.-C. Yin, H.-B. Yao, *Chem. Soc. Rev.* **2023**, *52*, 5516.
[17] M. Kazes, T. Udayabhaskararao, S. Dey, D. Oron, *Acc. Chem. Res.* **2021**, *54*, 1409.
[18] D. Choi, H. Kim, Y. Bae, S. Lim, T. Park, *ACS Energy Lett.* **2024**, *9*, 2633.
[19] A. Dey, J. Ye, A. De, E. Debroye, S. K. Ha, E. Bladt, A. S. Kshirsagar, Z. Wang, J. Yin, Y. Wang, L. N. Quan, F. Yan, M. Gao, X. Li, J. Shamsi, T. Debnath, M. Cao, M. A. Scheel, S. Kumar, J. A. Steele, M. Gerhard, L. Chouhan, K. Xu, X. Wu, Y. Li, Y. Zhang, A. Dutta, C. Han, I. Vincon, A. L. Rogach, et al., *ACS Nano* **2021**, *15*, 10775.
[20] J. Y. Kim, J. Lim, W. Jang, D. H. Wang, *Adv. Opt. Mater.* **2025**, *13*, 2403039.
[21] J. Y. Kim, B. G. Kim, M. Kim, W. Jang, D. H. Wang, *J. Alloys Compd.* **2021**, *886*, 161347.
[22] J. Y. Kim, W. Jang, T. Y. Im, D. H. Wang, *J. Alloys Compd.* **2025**, *1010*, 177990.
[23] Y. Dong, T. Qiao, D. Kim, D. Parobek, D. Rossi, D. H. Son, *Nano Lett.* **2018**, *18*, 3716.
[24] D. Yang, X. Li, W. Zhou, S. Zhang, C. Meng, Y. Wu, Y. Wang, H. Zeng, *Adv. Mater.* **2019**, *31*, 1900767.
[25] D. Li, C. Zhao, X. Zhang, X. Zhao, H. Huang, H. Li, F. Li, J. Yuan, *Adv. Mater.* **2025**, *37*, 2417346.
[26] K. Y. Jang, S. E. Chang, D.-H. Kim, E. Yoon, T.-W. Lee, *Adv. Mater.* **2025**, *37*, 2415648.
[27] M.-G. Jeon, G. H. An, A. Kirakosyan, S. Yun, J. Kim, C.-Y. Kim, H. S. Lee, J. Choi, *ACS Nano* **2024**, *18*, 29078.
[28] H. Li, X. Zhu, D. Zhang, Y. Gao, Y. Feng, Z. Ma, J. Huang, H. He, Z. Ye, X. Dai, *Nat. Commun.* **2024**, *15*, 6561.
[29] L. Protesescu, S. Yakunin, M. I. Bodnarchuk, F. Krieg, R. Caputo, C. H. Hendon, R. X. Yang, A. Walsh, M. V. Kovalenko, *Nano Lett.* **2015**, *15*, 3692.
[30] J. Song, J. Li, X. Li, L. Xu, Y. Dong, H. Zeng, *Adv. Mater.* **2015**, *27*, 7162.
[31] H. Li, Y. Feng, M. Zhu, Y. Gao, C. Fan, Q. Cui, Q. Cai, K. Yang, H. He, X. Dai, J. Huang, Z. Ye, *Nat. Nanotechnol.* **2024**, *19*, 638.
[32] N. Fiuza-Maneiro, J. Ye, S. K. Sharma, S. Chakraborty, S. Gómez-Graña, R. L. Z. Hoye, L. Polavarapu, *ACS Energy Lett.* **2025**, *10*, 1623.
[33] M. M. Byranvand, C. Otero-Martínez, J. Ye, W. Zuo, L. Manna, M. Saliba, R. L. Z. Hoye, L. Polavarapu, *Adv. Opt. Mater.* **2022**, *10*, 2200423.
[34] D. Chen, T. Wang, P. Kei Ko, J. Shi, M. Liu, J. E. Halpert, *Angew. Chemie Int. Ed.* **2024**, *63*, 202317590.
[35] Y. Liu, C. Tao, Y. Cao, L. Chen, S. Wang, P. Li, C. Wang, C. Liu, F. Ye, S. Hu, M. Xiao, Z. Gao, P. Gui, F. Yao, K. Dong, J. Li, X. Hu, H. Cong, S. Jia, T. Wang, J. Wang, G. Li, W. Huang, W. Ke, J. Wang, G. Fang, *Nat. Commun.* **2022**, *13*, 7425.
[36] W. Yin, M. Li, W. Dong, X. Zhang, W. Zheng, *Angew. Chem., Int. Ed.* **2023**, *62*, 202303462.
[37] J. Li, X. Hu, Y. Feng, X. Chen, J. Ye, X. Wang, C. Yang, D. Zhang, Q. Cai, H. He, Z. Ye, Q. He, X. Dai, J. Pan, *Nano Energy* **2025**, *140*, 111055.
[38] M. He, Q. Zhang, F. Carulli, A. Erroi, W. Wei, L. Kong, C. Yuan, Q. Wan, M. Liu, X. Liao, W. Zhan, L. Han, X. Guo, S. Brovelli, L. Li, *ACS Energy Lett.* **2023**, *8*, 151.

[39] Y. Xu, W. Guo, J. Yao, L. Xu, J. Wang, Z. Yang, S. Wang, J. Song, *Angew. Chem., Int. Ed.* **2025**, *64*, 202422823.

[40] P. Jha, N. Mukhin, A. Ghorai, H. Morshedian, R. B. Canty, F. Delgado-Licona, E. E. Brown, A. J. Pyrch, F. N. Castellano, M. Abolhasani, *Adv. Mater.* **2025**, *37*, 2419668.

[41] J. Zhang, D. Zhang, X. Zhou, L. Lian, C. Shen, C. Su, S. Fang, X. Liang, F. Yuan, L. Hou, Y.-X. Yuan, *Nano Lett.* **2024**, *24*, 12196.

[42] L. Wang, J. Liu, Y. Gong, J. Yu, Q. Li, Z. Liu, C. Zhang, S. Wang, X. Zhang, X. Yang, *Nano Lett.* **2024**, *24*, 7004.

[43] Y. Li, M. Deng, X. Zhang, T. Xu, X. Wang, Z. Yao, Q. Wang, L. Qian, C. Xiang, *Nat. Commun.* **2024**, *15*, 5696.

[44] J. Zhang, T. Zhang, Z. Ma, F. Yuan, X. Zhou, H. Wang, Z. Liu, J. Qing, H. Chen, X. Li, S. Su, J. Xie, Z. Shi, L. Hou, C. Shan, A. Multifunctional, *Adv. Mater.* **2023**, *35*, 2209002.

[45] H. Qi, Y. Tong, Y. Wang, Y. Liu, Z. Sheng, A. Kaisha, O. Toktarbaiuly, P. Pang, G. Xing, K. Wang, H. Wang, *Nano Lett.* **2025**, *25*, 353.

[46] X. Mei, J. Wang, X. Zhang, R. Zhuang, Y. Hua, K. He, W. Zheng, X. Zhang, *ACS Energy Lett.* **2023**, *8*, 4386.

[47] J. Zhang, B. Cai, X. Zhou, F. Yuan, C. Yin, H. Wang, H. Chen, X. Ji, X. Liang, C. Shen, Y. Wang, Z. Ma, J. Qing, Z. Shi, Z. Hu, L. Hou, H. Zeng, S. Bai, F. Gao, *Adv. Mater.* **2023**, *35*, 2303938.

[48] L. Kong, X. Zhang, C. Zhang, L. Wang, S. Wang, F. Cao, D. Zhao, A. L. Rogach, X. Yang, *Adv. Mater.* **2022**, *34*, 2205217.

[49] X. Jin, C. Wang, Y. Miao, P. Liu, J. Ji, M. Chang, B. Xu, M. Zhao, J. Tian, J. Guo, *Adv. Funct. Mater.* **2024**, *34*, 2401435.

[50] X. Li, X. Shen, Q. Lv, P. Guo, L. Xiao, *Coatings* **2024**, *14*, 83.

[51] W. Zhou, Y. Shen, L.-X. Cao, Y. Lu, Y.-Y. Tang, K. Zhang, H. Ren, F.-M. Xie, Y.-Q. Li, J.-X. Tang, *Adv. Funct. Mater.* **2023**, *33*, 2301425.

[52] Q. Lv, X. Shen, X. Li, J. Liu, Z. Shan, L. Xiao, P. Guo, J. C. Ho, *Nano Res.* **2025**, *18*, 94907119.

[53] X. Wang, Y. Ling, X. Lian, Y. Xin, K. B. Dhungana, F. Perez-Orive, J. Knox, Z. Chen, Y. Zhou, D. Beery, K. Hanson, J. Shi, S. Lin, H. Gao, *Nat. Commun.* **2019**, *10*, 695.

[54] Z. Wang, Y. Wei, Y. Chen, H. Zhang, D. Wang, J. Ke, Y. Liu, M. Hong, *Angew. Chem., Int. Ed.* **2024**, *63*, 202315841.

[55] Y. Song, S. Lan, B. Yang, Y. Zheng, Z. Zhou, C.-W. Nan, Y.-H. Lin, *J. Am. Chem. Soc.* **2024**, *146*, 19748.

[56] Z.-S. Liu, Y. Wang, F. Zhao, H.-H. Li, W.-Z. Liu, W.-S. Shen, H.-W. Duan, Y.-K. Wang, L.-S. Liao, *Light Sci. Appl.* **2025**, *14*, 35.

[57] Y.-K. Wang, H. Wan, S. Teale, L. Grater, F. Zhao, Z. Zhang, H.-W. Duan, M. Imran, S.-D. Wang, S. Hoogland, L.-S. Liao, *Nature* **2024**, *629*, 586.

[58] W. He, L. Kong, P. Yu, G. Yang, *Adv. Mater.* **2023**, *35*, 2209995.